
# Experimental and numerical fatigue assessment of duplex stainless-steel corrugated web I-girders

Engineering Structures 346 (2026) 121621

Contents lists available at ScienceDirect

Engineering Structures

journal homepage: www.elsevier.com/locate/engstruct

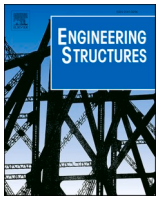

# Experimental and numerical fatigue assessment of duplex stainless-steel corrugated web I-girders

Fatima Hlal [a,b,*], Mohammad Al-Emrani [a]

[a] Department of Architecture and Civil Engineering, Chalmers University of Technology, Gothenburg, Sweden
[b] Bridge Department, WSP, Gothenburg, Sweden

ARTICLE INFO

*Keywords:*
Fatigue
Corrugated web
Duplex stainless steel
Effective notch stress
Hot spot stress

ABSTRACT

This paper investigates the fatigue behaviour of duplex stainless-steel (EN 1.4162) corrugated web beams. Thirteen beams, divided into two groups with different corrugation angles and radii, were tested under cyclic loading to failure. Additionally, one beam from each group was tested under static loading to estimate the hot spot stress (HSS) at the crack initiation location (S-point). The tests revealed two primary fatigue cracking modes: web cracking initiated at the web weld line within the shear span, and flange cracking initiated at the corrugation corners (S-points). A statistical evaluation of the developed flange cracks was conducted and compared with previously established detail categories (DC) for carbon steel using the nominal stress method. The tested beams exhibited fatigue strength comparable to carbon steel beams. Specifically, beams with a 45° corrugation angle corresponded to DC100, while beams with a ~30° corrugation angle corresponded to DC125. The estimated hot spot stress obtained from test measurements was used to validate the FE model. The fatigue test results were then evaluated using the hot spot stress (HSS) and effective notch stress (ENS) methods. The HSS method with DC100 and the ENS method with DC225, according to IIW guidelines, both based on the maximum principal stress component, provided conservative estimates of the fatigue strength of the tested beams.

## 1. Introduction

Corrugated web girders are becoming increasingly popular due to their high shear capacity and material efficiency [1–3]. The corrugated web design enables the use of thinner webs and reduces the need for stiffeners, which offer both economic and structural benefits [1]. Stainless steel has demonstrated significant advantages in bridge construction, particularly in terms of life cycle cost (LCC) [4–8], however, its high initial investment cost has limited its widespread usage in bridges [5]. Recent research highlighted that integrating corrugated webs into stainless steel I-girders presents a cost-effective design solution for road bridges [5, 9–11]. Corrugated webs can minimize material usage and production costs, which helps to bridge the cost gap between stainless steel and carbon steel while retaining stainless steel's long-term advantages, such as reduced maintenance costs and extended service life [10]. Fig. 1 Presents a case study comparing three bridge girder designs, in which the EN 1.4162 duplex stainless girder with corrugated webs achieved an 18 % lower life cycle cost than the conventional S355 flat web girder. The study highlights that potential savings can be even greater for deeper girders, higher average daily traffic (ADT), and more intensive paint maintenance schedules [10].

To enable the use of corrugated webs in bridge girders, it is essential to define detail categories (DC) that describe their fatigue strength. Corrugated webs introduce stress concentration points, typically located at the corners of the corrugations (the S-point in Fig. 2) [12–16]. The fatigue strength of such a welded detail is influenced by the corrugation configuration and the load effects that are distinct from those in flat web girders [17–19].

Extensive experimental and analytical work has been conducted and reported in the literature on the fatigue behaviour of carbon steel corrugated web I-girders. These experiments were conducted on beams subjected to 4-point bending, 3-point bending, or on axially loaded T-section elements. In previous work [20], the authors of this paper compiled a total of 86 fatigue tests, comprising 25 beams (CWGs) and 61 T-section members (CWTs). Statistical analysis of the tests that failed at the S-point below 5 million cycles led to the proposal of four fatigue detail categories based on the corrugation angle for carbon steel; DC125 for angles equal or smaller than 30°, DC112 for angles between 30° and 40°, DC100 for angles between 40° and 45°, and DC90 for angles between 45° and 60°.

* Correspondence to: Department of Architecture and Civil Engineering, Chalmers University of Technology, Sven Hultins gata 6, Gothenburg 412 96, Sweden.
*E-mail address:* fatima.hlal@chalmers.se (F. Hlal).

https://doi.org/10.1016/j.engstruct.2025.121621
Received 26 May 2025; Received in revised form 10 September 2025; Accepted 16 October 2025

A more recent study conducted by Zuo et al. [21] investigated the fatigue behaviour of 20 trapezoidal corrugated-web steel girders (TCWGs) made of steel grade Q355B, focusing on four groups with varying geometrical dimensions under four-point bending. The authors reported that 85 % of the initial cracks originated at the S-point in the tensile flange, while the remaining specimens showed cracks at the web, starting from the weld toe in the middle of a flat fold, referred to as the B-point in Fig. 2. The authors stated that variations in parameters such as corrugation geometry, specimen size, fillet weld leg size, and welding method-all of which influence fatigue strength—result in differing fatigue strengths of TCWGs with various structural details. Consequently, the study employed the hot spot stress method, which considers the influence of some of these factors and proposed DC130 based on the hot spot stress range. Additionally, the authors introduced formulae to estimate the stress concentration factors (SCFs) in relation to hot spot stress.

Although extensive research has been conducted on carbon steel corrugated web members, to the authors' knowledge, no experimental results are available for duplex stainless steel. EN 1993–1–9 [22] does not provide specific detail categories for beams with corrugated webs. In general, the standard specifies that the listed detail categories apply to all grades of structural steel, including stainless steels and unprotected weathering steels. However, previous studies indicated that higher-strength steels, such as duplex stainless steel, tend to exhibit superior fatigue performance [23, 24].

This paper presents an experimental investigation into the fatigue behaviour of 13 welded corrugated web beams made from duplex stainless steel EN 1.4162, featuring two different corrugation angles and radii. The observed fatigue crack modes are documented and analysed. Statistical evaluation is conducted using the nominal stress method and compared with established S–N curves for carbon steel from previous work [20]. Furthermore, the test results are presented in terms of effective notch and hot spot stress ranges and evaluated against detail categories DC225 and DC100 as defined by IIW.

## 2. Experimental program

To assess the fatigue behaviour of duplex stainless-steel corrugated web girders, 13 beams were designed, manufactured, and tested to failure. The following sections provide an overview of the test specimens, test setup, and test procedure conducted in this research work.

### 2.1. Test specimens

Two groups of corrugated web I-girders were designed with varying corrugation angles and bend radii to evaluate their fatigue performance. This design approach was based on findings from previous studies [25], which identified these two parameters as the most influential factors affecting the fatigue strength of the flange-to-web welded detail in corrugated web girders. The tested beams were made of duplex stainless steel EN1.4162. Group B included 7 beams (B1-B7), while Group C comprised 6 beams (C3-C8). Detailed dimensions and corrugation configurations are provided in Table 1, with schematic drawings shown in Fig. 3a for Group B and Fig. 3b for Group C. A photograph of the actual tested beams is presented in Fig. 3c.

With reference to the design of the test beams, the web thickness was kept at 5 mm due to production limitations related to sheet pressing. The flange width and thickness were designed to prevent local flange buckling and to closely resemble the characteristics of actual bridge I-girders. It was important to select a flange width that is noticeably larger than the corrugation depth for realistic stress distribution, as the large corrugation depth in relation to the flange width might lead to less accurate representations of stress concentrations at the corners of the corrugations. The beam height and length were chosen based on the loading capacity of the testing machine. To reduce localized effects from concentrated forces at the reaction points, two stiffeners with a thickness of 12 mm were added to each beam. However, no stiffeners were placed directly under the point loads to prevent potential stress concentrations that could result from their presence. Instead, the load was spread over a 50 mm area at each loading point, see Fig. 3.

The beams were welded manually with Gas Metal Arc Welding (GMAW). A weld throat thickness of 4 mm was used. The fabricator of the test beams was instructed to avoid the stop-start points in the pure bending area and one wave outside on each side of this region. Also, all the stop-start points were located on flat folds. Manual grinding was used to treat the stop-start points and at some weld points to reach weld Class B according to ISO5817. Although the aim was to produce fillet welds, the small web thickness (5 mm) and welding from both sides resulted in full penetration welds. This was verified through cross-sections taken from welded specimens during welding trials.

The steel plates were procured from a stainless-steel manufacturer in Sweden. Web plates were corrugated by two different producers of corrugated web beams, and final beam welding was carried out at one of these companies. Laboratory measurements showed that Corrugation Group B met the tolerance requirements specified in SS-EN 1090–2:2018 [26]. Corrugation Group C met the specified tolerances for flange width and beam height; however, variations were observed in the bending radius—approximately 20 mm—and in the corrugation angles, which ranged between 27° and 31°, deviating by −4° to −9° from the intended value (35°). Additionally, web eccentricity (the offset between the web and flange centrelines) showed a deviation of 4–8 mm along the beam.

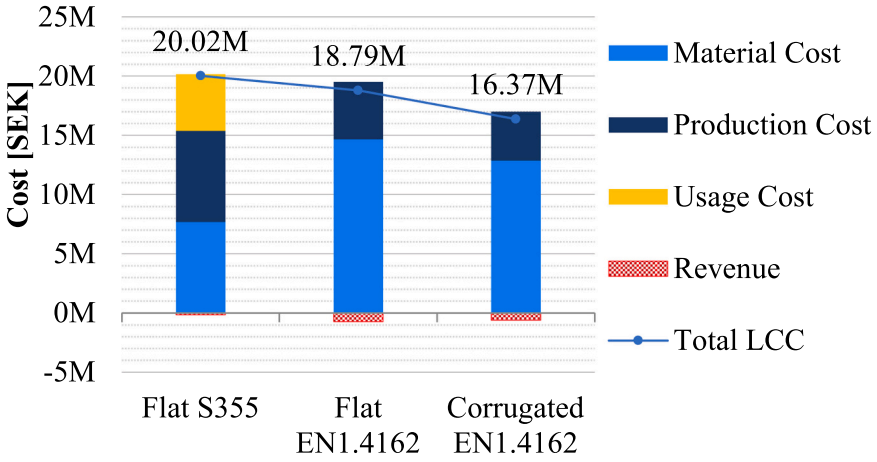


**Fig. 1.** LCC comparison for three optimized design solutions for a case study bridge. Sourced from [10].

### 2.2. Test setup

The beams were tested under four-point bending with bearings providing simply supported conditions. Each test involved two beams being tested simultaneously, with the load applied using two hydraulic jacks with a load control system. The loading setup is illustrated in Fig. 4, showing the actual test setup in Fig. 4a, and a schematic drawing that highlights the load application principle in Fig. 4b. Two beams were tested simultaneously in each run, as the setup was specifically designed to accommodate paired specimens. The load was applied by pressing the top and bottom beams toward each other (see Fig. 4b) which tension the top side of the bottom beam and the bottom side of the top beam. When one beam failed, it was replaced by a dummy beam. Before loading, the bottom beam and the load cell were hung on the top beam. The resulting preload was estimated to be around 4 kN per point, which is negligible compared to the applied fatigue load and unlikely to affect the results significantly. Fatigue cracks initiated either in the top beam first (e.g., specimen B3) or in both beams simultaneously (e.g., specimens B5 and B6).

In the experimental setup, beams in Group B had a non-integer number of corrugations in the shear span, 2.5 corrugation waves, whereas Group C beams had 2 corrugation waves, as depicted in Fig. 3. According to the study conducted by Hlal and Al-Emrani [17], this setup would result in transverse bending due to shear flow also in the pure bending region of Group B beams. Conversely, such bending is not anticipated in Group C due to the integer number of corrugation waves within the shear span. However, considering the substantial flange width in relation to the corrugation depth, the effect of this transverse bending is expected to be minimal at the corrugation corner (crack initiation location).

To quantify both the transverse bending and the membrane bending stress experimentally, two uniaxial strain gauges with a 20 mm grid length were installed on both flange edges at the centre of the beam in the pure bending region, positioned on the top surface of the bottom flange, and placed 15 mm from the flange edge. In Fig. 5a, the strain gauges S1-D and S2-D are shown for a representative beam from Group B, while Fig. 5b illustrates the corresponding setup for a representative beam from Group C. Both subfigures also present the numbering scheme applied to each group. Moreover, strain gauges S1B to S4B (Figure 5a) and S1C to S4C (Fig. 5b) —shown in the zoomed-in details— were used to measure the hot spot stresses in Group B and Group C, respectively. These four axial strain gauges, each with a grid length of 0.6 mm, were installed on opposite sides of the pure bending region of beams B4 and C5 (one beam from each group), as illustrated in Fig. 5. The gauges were positioned at distances of 0.4 t (8 mm) and 1.0 t (20 mm) from the weld toe, where t denotes flange thickness, in accordance with the IIW linear extrapolation method.

With reference to crack detection, twelve uniaxial strain gauges, each with a grid length of 50 mm (referred to as S1-C to S12-C in Fig. 5), were placed at the corrugation corners within the pure bending region and the first corrugation on each side of this area, where flange fatigue cracks are expected to develop. These strain gauges were installed on the first tested beams (B1 to B4) to monitor crack propagation and to stop the test for these beams when a considerable change in the gauge reading is observed. At the same time, throughout the test, the load cells' deflection was continuously monitored. It was observed that deflection changes were minimal for most of the test duration, with changes only becoming noticeable when the crack grew through the thickness of the flange plate. It was also observed that the number of cycles between the detection of surface cracks, identified through strain gauge measurements, and the development of through-thickness cracks, detected by the deflection measurements, accounted for approximately 3–4 % of the total fatigue life. For the remaining beams, a deflection-based safety switch was implemented, designed to stop the loading actuator if deflection exceeded a specified limit. This limit allowed for an increase of approximately 1 % (0.5 mm over 38.5 mm) beyond the stable deflection established at 4000 cycles. All observed surface and through-thickness cracks were recorded and incorporated into the fatigue assessment.

**Table 1**
Detailed dimensions of the tested beams (units are in mm).

| Group | Cross-section | | | | | Corrugation configuration | | | |
|---|---|---|---|---|---|---|---|---|---|
| | $b_f$ | $t_f$ | $h_w$ | $h$ | $t_w$ | $a_1$ | $a_3$ | $\alpha$ | $R$ |
| B | 220 | 20 | 276 | 316 | 5 | 140 | 50 | 45° | 30 |
| C | 220 | 20 | 276 | 316 | 5 | 170 | 60 | 35° (27° to 31°) | 100 |

### 2.3. Test procedure

Before initiating cyclic loading, a static load step was carried out to monitor strain development in the pure bending region of both types of tested beams. In this step, the load was gradually increased to 300 kN for Beam B2 and 240 kN for Beam C5. Strain readings were taken using gauges S1-D and S2-D and used to estimate the membrane stress ($\sigma_m$) and transverse bending stress ($\sigma_b$) in the pure bending region.

The stresses were estimated using the following expressions: $\sigma_m = \frac{\varepsilon_{S1-D}+\varepsilon_{S2-D}}{2} * E$, $\sigma_b = \frac{\varepsilon_{S1-D}-\varepsilon_{S2-D}}{2} * E$. Where E is the modulus of elasticity, assumed to be 200 GPa, and $\varepsilon_{S1-D}$, $\varepsilon_{S2-D}$ are the strains recorded by gauges S1-D and S2-D, respectively. The bending stress at the corrugation corner is then calculated as $\sigma_{b.corner} = \sigma_b * \frac{a_3}{b_f}$ where $a_3$ is the corrugation depth and $b_f$ is the flange width.

The results for beam B2 are presented in Fig. 6a, and those for beam C5 are shown in Fig. 6b, alongside theoretical membrane stress calculated based on beam theory, excluding the web contribution to the section modulus. The membrane stress derived from strain measurements agreed well with the stress calculated according to beam theory.

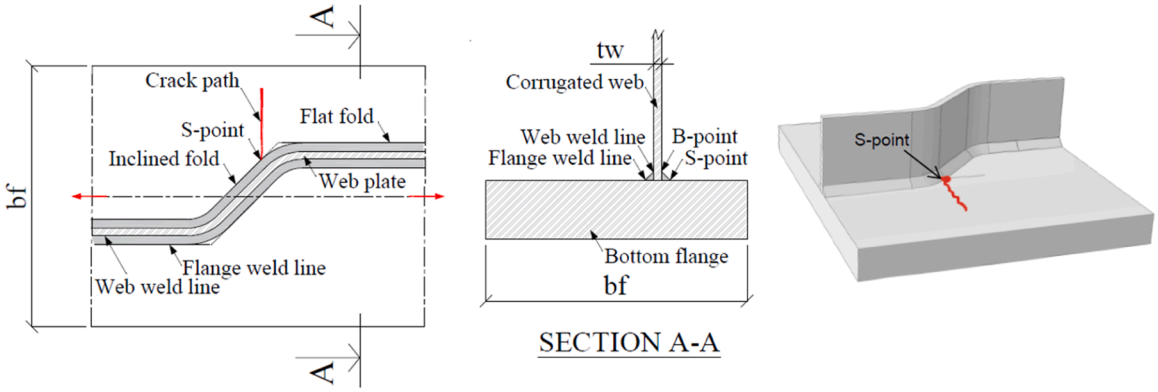


**Fig. 2.** Typical location of fatigue crack in corrugated web girders.

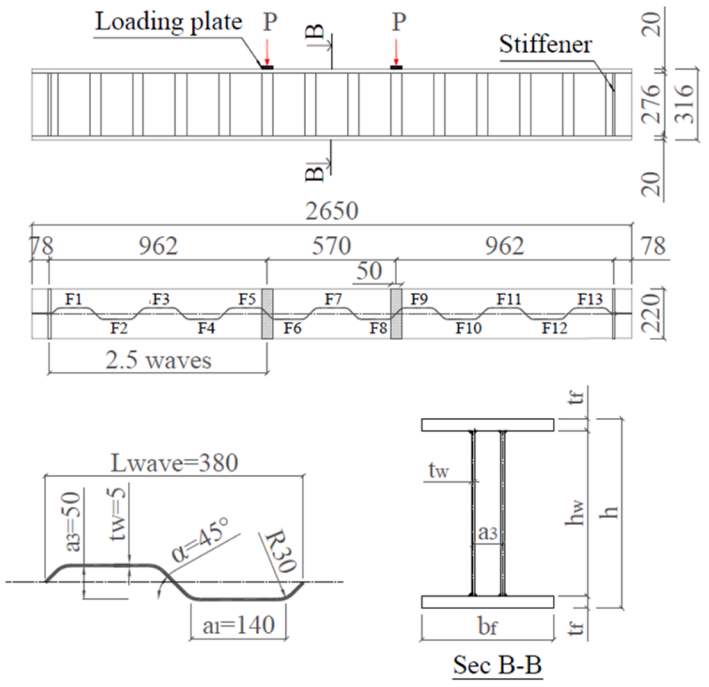


(a) B group dimensions

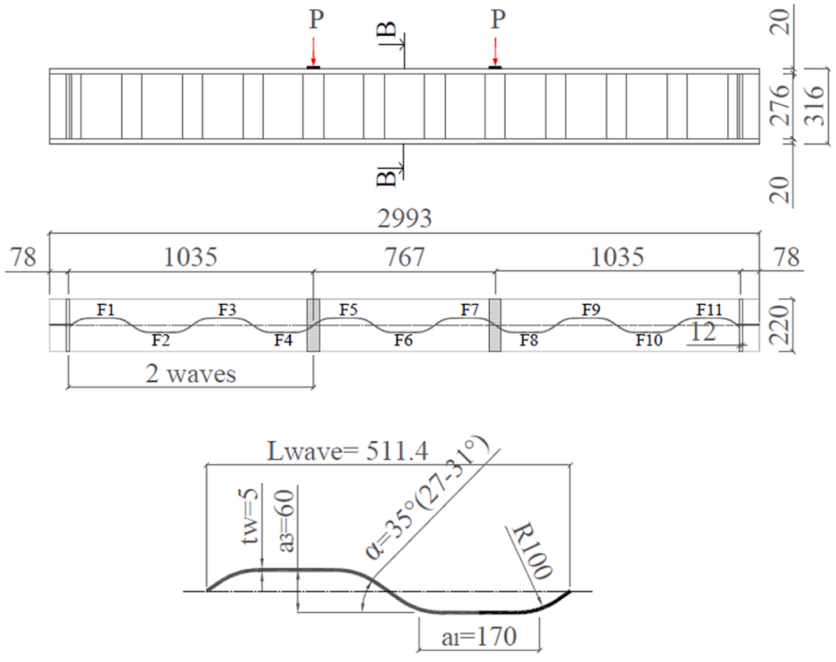


(b) C group dimensions

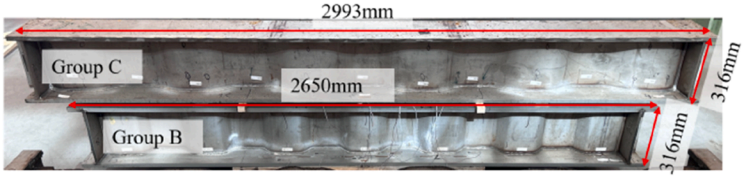


(c) Photograph showing two beams of the two tested groups

**Fig. 3.** Dimensions and geometric notations of the tested beams.

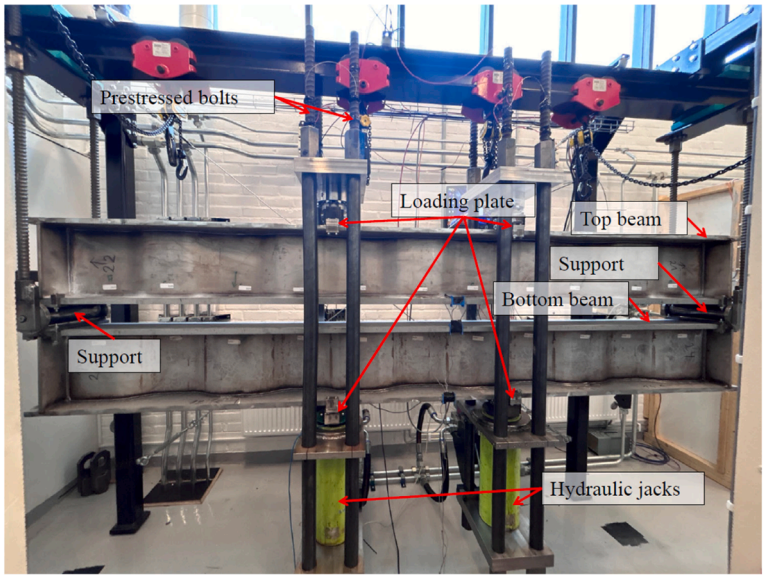


(a) The actual test setup

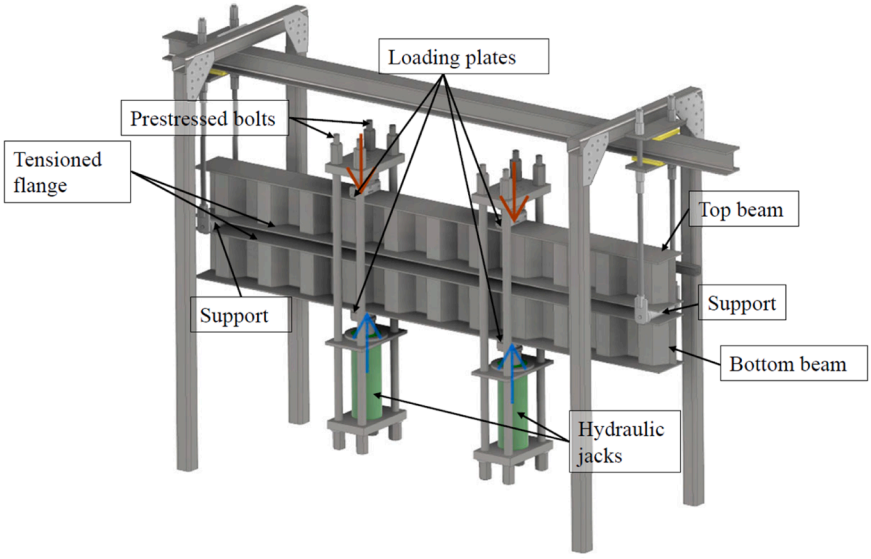


(b) Schematic illustration of the test setup

**Fig. 4.** Illustration of test setup.

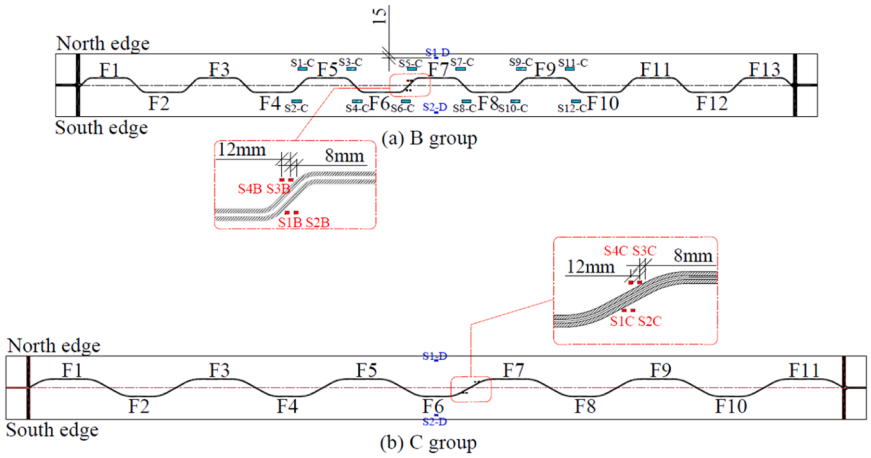


**Fig. 5.** Numbering scheme of the test beams.

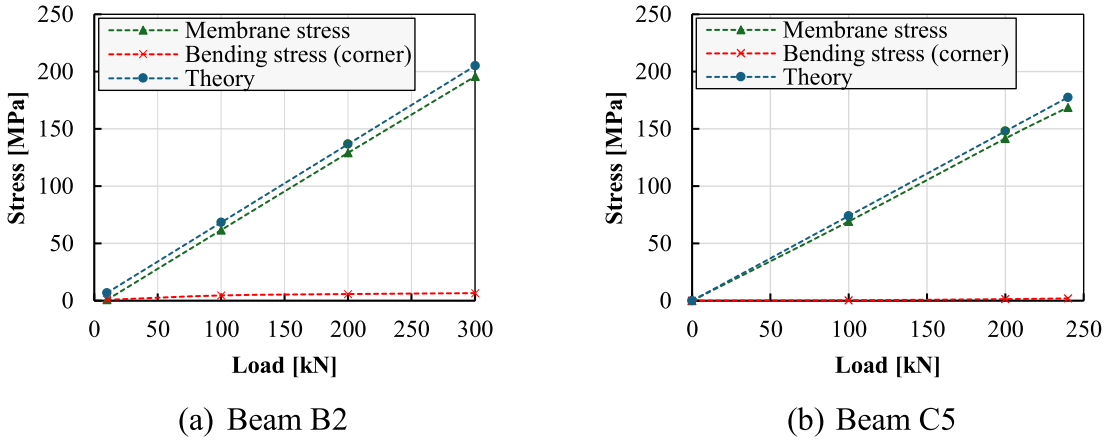


**Fig. 6.** Load versus membrane and transverse bending stress under static load before fatigue loading. E = 200 GPa.

Additionally, the maximum transverse bending stress derived from strain measurements $\sigma_{b.corner}$ was minimal, only 3 % of the membrane stress in Group B and 1 % in Group C, due to the wide flange relative to the corrugation depth. As a result, the theoretical membrane stress $M/W$ was used as the basis for nominal stress calculations in the fatigue assessment.

Cyclic loading was applied at a frequency of 3.8 Hz (228 cycles/min). The maximum applied fatigue load ($P_{\max}$) was set to 52 % of the girder's capacity, which is estimated to be 575 kN per point based on flange yielding. The minimum load ($P_{\min}$) was chosen to achieve a stress ratio of R = 0.1. Table 2 provides a summary of the fatigue loading matrix. Each group was tested under different stress ranges to establish the SN curve for the respective group.

## 3. Finite element modelling

### 3.1. FE model description

Two finite element (FE) models of the two tested groups were built using ABAQUS CAE2023, based on the dimensions provided in Fig. 3. The modelling process involved three sequential stages. First, a global model was constructed to represent a simply supported beam, with the boundary conditions illustrated in Fig. 7 and detailed in Table 3. In the testing machine, the load is applied to a 50 mm loading plate. To resemble this, the flange surface was partitioned at the loading positions, creating area A in Fig. 7. A reference point was defined at the centre of each partitioned area, and all surface nodes within the area were linked to the reference point using a multi-point constraint (MPC). The load was then applied directly at the reference point. The global model was meshed using quadratic tetrahedral solid elements (C3D10) with an approximate global element size of 10 mm. Validation of this model is provided in Section ↱3.2.

Next, a sub-model was created to capture the hot spot stress (HSS), referred to as the *HSS sub-model,* in Fig. 7. This sub-model included a half corrugation wave, aiming to capture the stress concentration near the weld line. The faces of this sub-model were connected to the global model through the "Submodel" boundary condition feature in ABAQUS. This feature is a special type of boundary condition that links a sub-model (a smaller, detailed model) to a global model (the full structure). It transfers nodal displacements from the global model to the boundaries of the sub model, ensuring that the sub-model responds as if it is still part of the full structure. At this stage, the weld geometry was explicitly modelled using nominal dimensions, with a 4 mm throat thickness and no penetration. The surfaces where the hot spot stresses were to be obtained were partitioned in accordance with the guidelines of IIW. The studied detail is of Type a (weld toe on the plate surface). A mesh convergence study, along with two extrapolation methods—linear and quadratic—was conducted. The results are presented in Table 4. The mesh convergence study demonstrated that using three elements between 0 t and 0.4 t, and five elements between 0.4 t and 1.0 t, provides good accuracy for hot spot stress calculations. Additionally, the results from linear and quadratic extrapolation methods were found to be close. Consequently, in alignment with the test measurement points, linear extrapolation was selected for use in the subsequent analysis. The maximum principal stress was also compared with the longitudinal stress in the flange. The results showed a close alignment, with differences of less than 1 %, indicating that the maximum principal stress is oriented in the same direction as the longitudinal stress. Additionally, the angle between the maximum principal stress (or longitudinal stress) and the line perpendicular to the weld line is 60 degrees for a corrugation angle of 30 degrees, and 45 degrees for a corrugation angle of 45 degrees, which are within the range ±60° specified by IIW.

Finally, a sub-model for effective notch stress (ENS) was created; referred to as (*ENS sub-model)* in Fig. 7. It captures a single corrugation corner, including the critical S-point region. This model requires a finer mesh and detailed modelling of the weld notch. The weld configuration was modelled following IIW guidelines, with the weld toe and root rounded with a radius of r = 1 mm (plate thickness >=5 mm). Both the web weld line and the flange weld line (see Table 5) are rounded to assess the effective notch stress (ENS) on the web and flange sides of the fillet weld. Like the previous models, quadratic tetrahedral solid elements (C3D10) were used. A mesh convergence study is also conducted and presented in Table 5. Element size 0.25 mm inside the root and toe regions, gradually increasing to 3 mm towards the outer edges, captures the effective notch stress with good accuracy.

Both the *HSS sub-model* and the *ENS sub-model* were moved along the

**Table 2**
Summary of Test Program.

| Beam | $P_{max}$ [kN/point] | $P_{min}$ [kN/point] | $P_{max}/P_{yield}$ [-] | $\Delta\sigma_m = M/W$ [MPa] |
|---|---|---|---|---|
| B1 | 300 | 30 | 52 % | 185.7 |
| B2 | 300 | 30 | 52 % | 185.7 |
| B3 | 300 | 30 | 52 % | 185.7 |
| B4 | 300 | 30 | 52 % | 185.7 |
| B5 | 220 | 22 | 38 % | 136.2 |
| B6 | 220 | 22 | 38 % | 136.2 |
| B7 | 220 | 22 | 38 % | 136.2 |
| C3 | 205 | 20.5 | 36 % | 136.5 |
| C4 | 240 | 24 | 42 % | 159.8 |
| C5 | 205 | 20.5 | 36 % | 136.5 |
| C6 | 250 | 25 | 43 % | 166.4 |
| C7 | 250 | 25 | 43 % | 166.4 |
| C8 | 240 | 24 | 42 % | 159.8 |

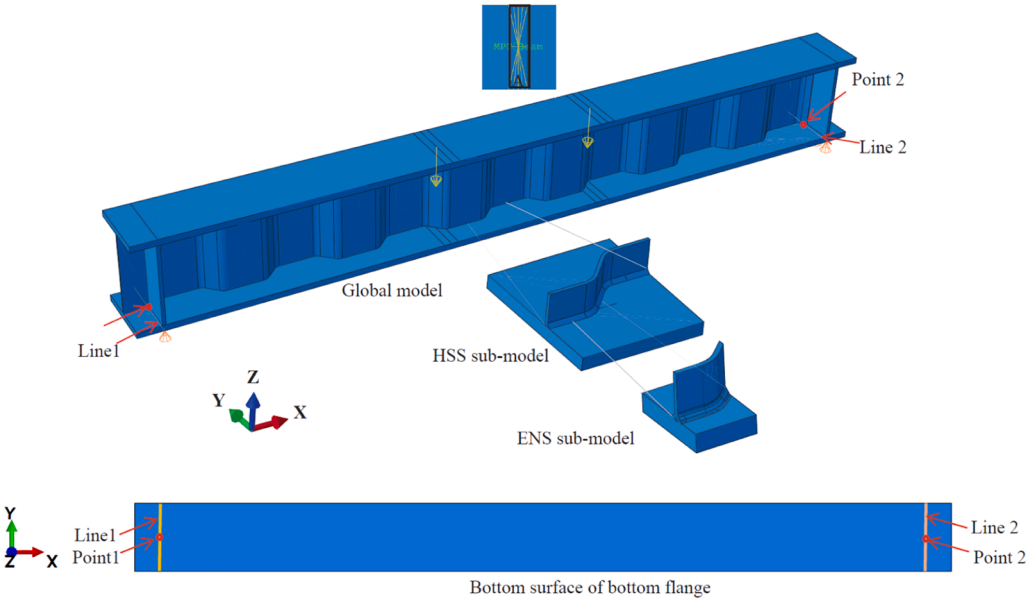


**Fig. 7.** Illustration of the global model, hot spot sub model, effective notch sub model, and the applied boundary conditions.

**Table 3**
Applied boundary conditions on the global model. Refer to Fig. 7 for annotations.

| | *Ux* | *Uy* | *Uz* | *URx* | *URy* | *URz* |
|---|---|---|---|---|---|---|
| Line 1 | 1 | 1 | 0 | 1 | 1 | 1 |
| Line 2 | 1 | 1 | 0 | 1 | 1 | 1 |
| Point 1 | 0 | 0 | 1 | 1 | 1 | 1 |
| Point 2 | 1 | 0 | 1 | 1 | 1 | 1 |

corrugation corners to extract hot spot stress/effective notch stress values at any corrugation corner, enabling comprehensive stress evaluation along the beam.

### 3.2. FE-model validation

As mentioned in Section ↱2.2, membrane and transverse bending stresses, as well as hot spot stresses at two opposite corners in the pure bending region, were derived from strain measurements on one beam from each group. The results were compared to those obtained from the FE-models and presented in Table 6, which shows good agreement. For Beam C5, the nominal stress was calculated as the average of the measured values from S1-D and S2-D. In the case of beam B4, flange edge strains were obtained using fibre optic sensors placed on the top surface of the bottom flange. Further details on the measurement setup for beam B4 can be found in [27].

## 4. Fatigue test results

The tested beams developed two distinct types of fatigue cracking: web cracks and flange cracks. Examples of these cracks are presented in Fig. 8. Beams B1 and B2 showed web cracks, whereas the remaining beams developed flange cracks. Web cracks emerged within the shear span where bending and shear forces are present, while flange cracks primarily formed in the region of pure bending, and half a corrugation beyond each point load towards the supports.

### 4.1. Web cracks

The chosen specimen dimensions, characterized by a short web

**Table 4**
Mesh sensitivity on HSS (applied load 260kN/point), max principal stress component. Sub model located at F6–F7 position of Group B.

| Mesh layout | 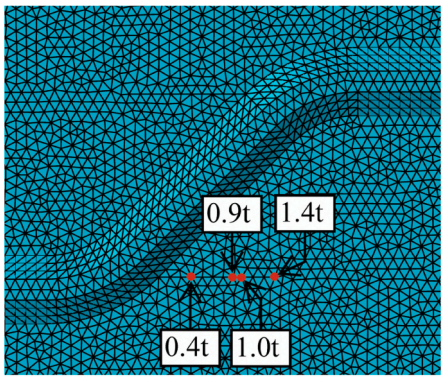 | 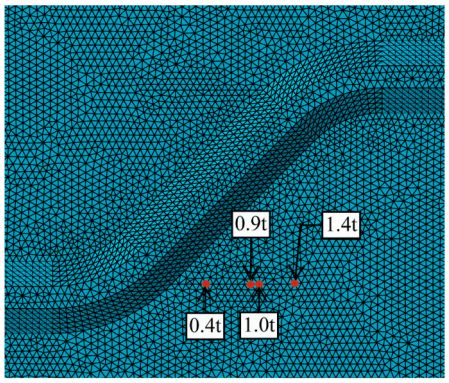 |
|---|---|---|
| Element size | ≈ 2.5 mm | ≈ 1.5 mm |
| $HSS_{Linear}$ | 198.4 MPa | 199.4 MPa |
| $HSS_{Quadratic}$ | 203.8 MPa | 205.1 MPa |
| Difference | 2.6 % | 2.7 % |

**Table 5**
Mesh sensitivity on ENS (applied load 260kN/point), max principal stress component. Sub model located at the south corner of F6–F7 position in Group B.

| | | |
|---|---|---|
| Mesh layout | 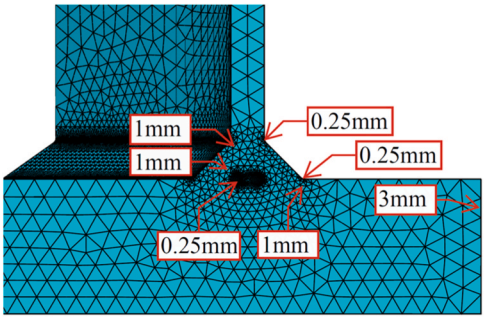 | 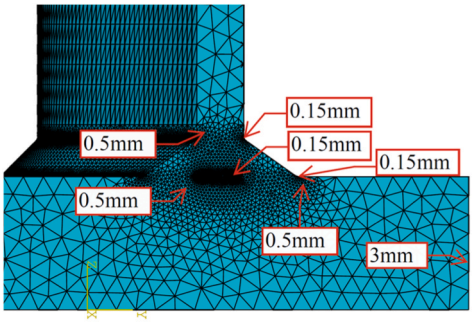 |
| $ENS_{S-point}$ | 395.2 MPa | 396.47 MPa |

**Table 6**
Numerical results compared to experimental results. E = 200 GPa.

| | Load/point | Location | $NS_{EXP}$ | $HSS_{EXP}$ | $SCF_{EXP}$ | $NS_{FE}$ | $HSS_{FE}$ | $NS_{EXP}/NS_{FE}$ | $HSS_{EXP}/HSS_{FE}$ |
|---|---|---|---|---|---|---|---|---|---|
| Group B | 95 kN | F6-7N | 61.25 | 83.16 | 1.36 | 65.1 | 80.5 | 94 % | 103 % |
| | | F6–7S | 57.13 | 76.23 | 1.33 | 60.37 | 72.5 | 95 % | 105 % |
| Group C | 100 kN | F6-7N | 69.17 | 82.82 | 1.20 | 71.17 | 78.6 | 97 % | 105 % |
| | | F6–7S | 69.17 | 81.03 | 1.17 | 71.17 | 81.7 | 97 % | 99 % |

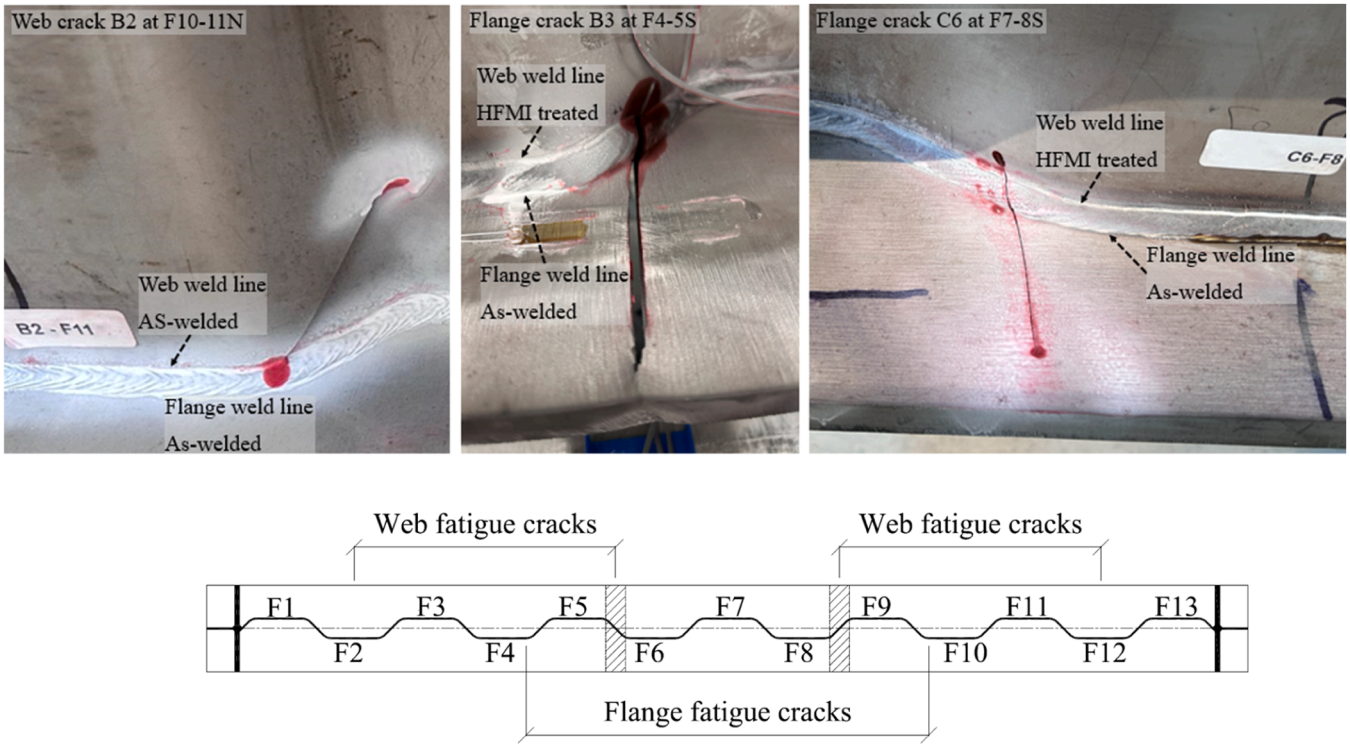


**Fig. 8.** Obtained fatigue cracking modes.

height and a wide, thick flange plate, led to a combined effect of high shear flow and normal stress at the flange-to-web weld line in the shear span, thereby increasing the risk of fatigue failure in the web plate. Beams B1 and B2 displayed this type of cracking with three web cracks in each beam. The cracks initiated at the web weld line in the corrugation corners and propagated toward the inclined fold at an angle of approximately 50 degrees, see Fig. 8 and Fig. 9. Similar web cracking modes were reported in a recent experimental study conducted by Zuo et al. [21]. The stress versus number of cycles to failure for the observed web cracks in Group B is summarized in Table 7.

For the remaining beams of both groups, the web weld line (Fig. 2 & Fig. 8) along the beam length was treated with high-frequency mechanical impact (HFMI). This treatment enhanced the fatigue life of web cracks originating at the web weld line. As a result, in the remaining beams, fatigue cracks were expected to initiate at the flange weld line, particularly in the pure bending region where the maximum normal stress is present.

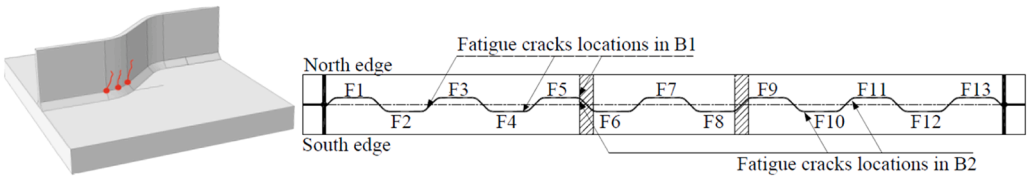


**Fig. 9.** Web fatigue crack locations in B1&B2.

**Table 7**
Stress versus number of cycles to failure for web fatigue cracks.

| | location | Bending stress [MPa] | Shear stress [MPa] | N [Cycles] |
|---|---|---|---|---|
| B1 | F5-F6N | 185.7 | 169.8 | 478443 |
| B1 | F4-F5S | 141.8 | 169.8 | 478443 |
| B1 | F2-F3S | 70.66 | 169.8 | 478443 |
| B2 | F10-F11N | 105.1 | 169.8 | 478444 |
| B2 | F9-F10S | 141.8 | 169.8 | 478445 |
| B2 | F5-F6N | 185.7 | 169.8 | 478446 |

### 4.2. Flange cracks

Flange cracks primarily developed in the pure bending region; however, 8 out of 29 cracks observed in all beams occurred in the shear span, indicating comparable or even higher local stress levels in this area relative to the pure bending region. This observation aligns with the finite element results, which revealed elevated hot spot stress and effective notch stress at the corners F9–10S & F4–5S in Group B and F8–9N & F3–4N in Group C. This phenomenon is thought to be attributed to the specific dimensions of the tested beams, characterized by a thin and short web in contrast to thick and wide flanges, which are not typical for steel bridge girders. These dimensions led to local distortion and magnified load effects in the shear span, which is also confirmed in the finite element models of both Group B and C. To investigate this further, a finite element (FE) model was created for Group C, maintaining the same corrugation configuration while adjusting the web height and the beam span to 1 m and 5.4 m, respectively. The 1m-deep girder model yielded an identical stress concentration factor in the pure bending area as the test specimen and showed the highest effective notch stress (ENS) in this area. Consequently, for the fatigue assessment using the nominal stress method, which does not capture local load effects, only cracks originating in the pure bending region were included in the statistical analysis. In order to avoid fatigue cracking due to local distortion outside the constant moment region in the beams of Group C, HFMI treatment was used at these locations (F8–9N and F3–4N), and all cracks in this series initiated, consequently, in the constant moment region.

Beams B3 to B7 and four beams from Group C (C4, C6, C7, and C8) exhibited flange fatigue cracking at the S-point, while Beams C3 and C5 completed 5.4 million cycles without fatigue failure. Most failed beams developed multiple cracks, ranging from surface cracks to through-thickness cracks and those propagating to the flange edge. Crack propagation in beam B4 at F8–9N was closely monitored and presented in Fig. 10. The first detected crack appeared as a 17 mm surface crack after 453,623 load cycles, originating at the S-point and oriented nearly perpendicular to the direction of maximum principal stress (i.e., the longitudinal axis of the flange). The crack penetrated through the thickness after an additional 9353 cycles (approximately 2 % of the total fatigue life) and reached the flange edge after 22,013 cycles (about 4.5 % of the total fatigue life). Similarly, for Group C, the surface crack in beam C7 was first detected at 1116,507 cycles, penetrated through the thickness at 1170,419 cycles, and reached the flange edge at 1193,158 cycles, with about 6 % of the fatigue life from surface crack to flange edge. All observed cracks and their progression stages are summarized in Table 8.

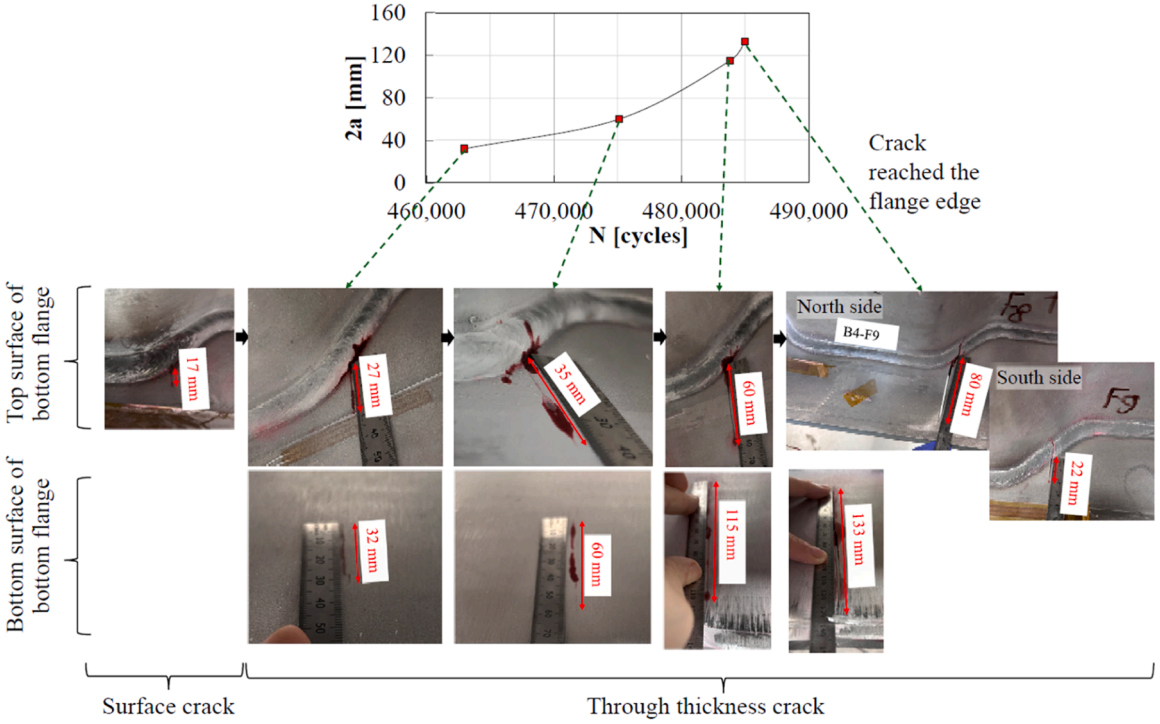


**Fig. 10.** Crack propagation at F8–9N in B4.

Furthermore, an early crack, depicted in Fig. 11, was detected in beam C4. A core sample was extracted from the fatigue crack location, and the examination of the fracture surface revealed that this crack originated from a weld defect (cold lap), which resulted in early cracking.

## 5. Evaluation of fatigue test results

### 5.1. Web cracks

The evaluation of the web fatigue cracks, developed in beams B1 and B2, is presented in Fig. 12. Initially, the effective notch stress at the crack locations was extracted from the finite element model and plotted against the fatigue life obtained from the experiment. The FE analysis indicated that the locations where the cracks developed correspond to the maximum effective notch stress values, with results presented in Fig. 12a showing that all data points are well above the SN curve for DC225.

As the web base metal at the crack initiation location is subjected to a combined action of normal and shear stresses, EC3 specifies that, for combined stress ranges, the fatigue damage at a point should be determined by separately combining the fatigue damage caused by different stress components [22–28]. For double-sided manual butt or fillet welds and for shear in the base metal, EN1993–1–9 specifies DC100. The fatigue life is calculated by assuming a damage sum equal to one, as per Eq. 1, and the results are compared to the test results in Fig. 12b. As can be noted, the EN1993–1–9 approach yields conservative results for the tested beams.

$$\frac{n}{N_{shear}} + \frac{n}{N_{normal}} = 1 \quad (1)$$

In Eq. 1, n represents the number of loading cycles that result in fatigue damage equal to 1.0 when subjected to a combination of shear and normal stress. $N_{shear}$ and $N_{normal}$ denote the number of loading cycles that lead to fatigue damage equal to 1.0 under shear and normal stress, respectively, when considered separately.

### 5.2. Flange cracks

The assessment of flange cracks is conducted using three fatigue assessment methods: nominal stress, hot spot stress, and effective notch stress methods. In relation to the fatigue assessment using the nominal stress method, a statistical evaluation in accordance with Eurocode [29] is conducted on the cracks that developed exclusively in the pure bending region, as elaborated in Section ↱4. The results are presented in Fig. 13, with Group B shown in Fig. 13a and Group C in Fig. 13b.

The statistical evaluation of the thirteen developed cracks in the pure bending region of Group B yielded characteristic DC104, while the seven cracks developed in Group C yielded DC127. These values can be rounded to DC100 and DC125 as per standard detail categories in EN1993–1–9. This finding aligns with the detail categories previously proposed in [20] for carbon steel beams with 45° and 30° corrugation angles. It is important to note that beam C4 was excluded from the statistical analysis due to early failure resulting from a local weld defect. If this beam had been included, Group C would have resulted in a characteristic strength of DC121 MPa.

Furthermore, a comparison of the previous carbon steel test data with the current tests on duplex stainless steel EN 1.4162, plotted with EC3 standard detail categories, is carried out and presented in Fig. 14.

All flange cracks that developed in both the pure bending region and the combined shear and bending region were assessed using the HSS method, except for the crack in beam C4. The HSS values were derived from numerical models, as detailed in Section ↱3. The HSS sub-model was moved to the crack location, and the corresponding hot spot stress was calculated. Fig. 15a presents the results alongside the DC100 fatigue class recommended by the IIW for non-load-carrying fillet welds.

**Table 8**
Stress and number of cycles to failure for flange fatigue cracks.

| | location | $\sigma$[MPa] $= M/W$ | N (cycles) | Region | Crack Development | Initiation location |
|---|---|---|---|---|---|---|
| B3 | F4–5S | 148.6 | 4.45E+ 05 | Combined shear and bending | Main crack | S-point |
| B3 | F5-6N | 185.7 | 4.45E+ 05 | Pure bending | Surface crack | S-point |
| B3 | F6–7S | 185.7 | 4.45E+ 05 | Pure bending | Surface crack | S-point |
| B3 | F8-9N | 185.7 | 4.45E+ 05 | Pure bending | Surface crack | S-point |
| B3 | F9–10S | 148.6 | 4.45E+ 05 | Combined shear and bending | Surface crack | S-point |
| B3 | F10-11N | 110.3 | 4.45E+ 05 | Combined shear and bending | Surface crack (local weld defect) | S-point |
| B4 | F8-9N | 185.7 | 4.85E+ 05 | Pure bending | Main crack | S-point |
| B4 | F9–10S | 148.6 | 4.85E+ 05 | Combined shear and bending | Through thickness | S-point |
| B4 | F4–5S | 148.6 | 4.85E+ 05 | Combined shear and bending | Through thickness | S-point |
| B4 | F6-7N | 185.7 | 4.85E+ 05 | Pure bending | Surface crack | S-point |
| B4 | F6–7S | 185.7 | 4.85E+ 05 | Pure bending | Surface crack | S-point |
| B5 | F4–5S | 109.0 | 1.11E+ 06 | Combined shear and bending | Surface crack | S-point |
| B5 | F6-7N | 136.2 | 1.11E+ 06 | Pure bending | Surface crack | S-point |
| B5 | F8-9N | 136.2 | 1.11E+ 06 | Pure bending | Through thickness | S-point |
| B5 | F9–10S | 109.0 | 1.11E+ 06 | Combined shear and bending | Surface crack | S-point |
| B6 | F6-7N | 136.2 | 1.11E+ 06 | Pure bending | Surface crack | S-point |
| B6 | F6–7S | 136.2 | 1.11E+ 06 | Pure bending | Surface crack | S-point |
| B6 | F8-9N | 136.2 | 1.11E+ 06 | Pure bending | Through thickness | S-point |
| B7 | F8-9N | 136.2 | 9.06E+ 05 | Pure bending | Main crack | S-point |
| B7 | F6-7N | 136.2 | 9.06E+ 05 | Pure bending | Surface crack | S-point |
| B7 | F4–5S | 109.0 | 9.06E+ 05 | Combined shear and bending | Surface crack | S-point |
| C3 | "-" | 136.5 | 5443246 | No cracks | Runout | "-" |
| C5 | "-" | 136.5 | 5443246 | No cracks | Runout | "-" |
| C6 | F7–8S | 166.4 | 1116507 | Pure bending | Main crack | S-point |
| C6 | F5-6N | 166.4 | 1116507 | Pure bending | Surface crack | S-point |
| C6 | F4–5S | 166.4 | 1116507 | Pure bending | Surface crack | S-point |
| C6 | F6–7S | 166.4 | 1116507 | Pure bending | Surface crack | S-point |
| C7 | F6–7S | 166.4 | 1193158 | Pure bending | Main crack | S-point |
| C7 | F7–8S | 166.4 | 1193158 | Pure bending | Through thickness | S-point |
| C4* | F4–5S | 159.8 | 952498 | Pure bending | Main crack | S-point |
| C8 | F7–8S | 159.9 | 1839857 | Pure bending | Surface crack | S-point |

* This beam was excluded from the statistical analysis due to a weld defect (cold lap) that resulted in early cracking

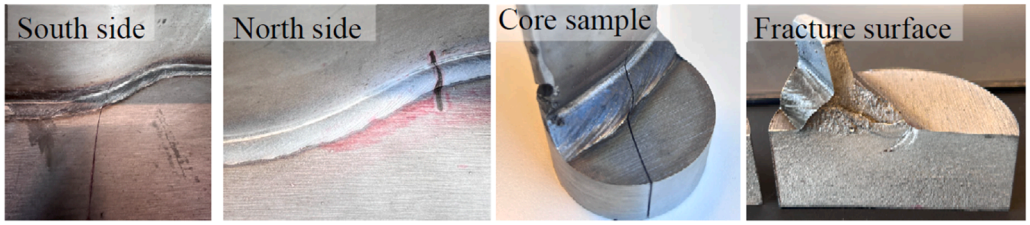


**Fig. 11.** Early fatigue cracking of beam C4.

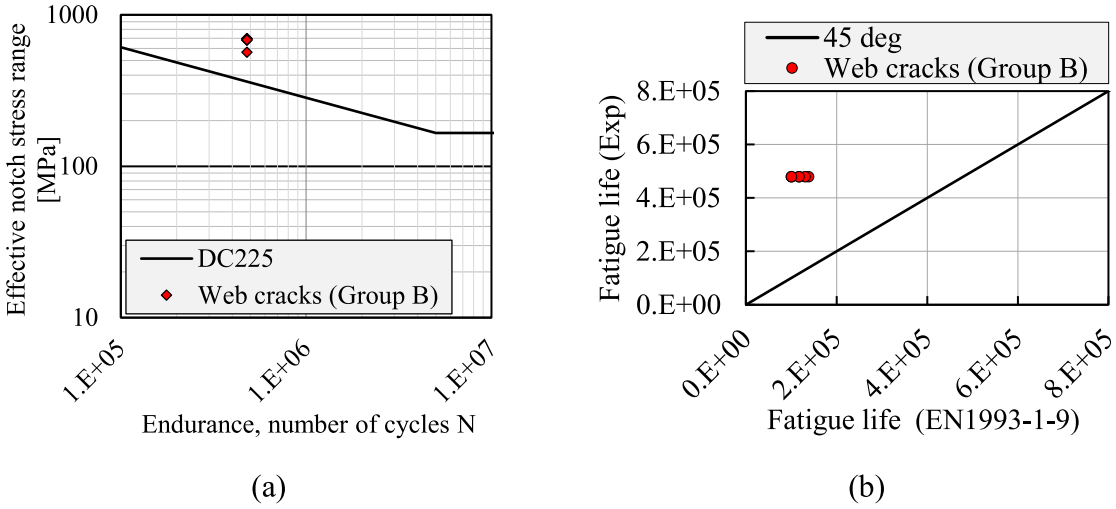


**Fig. 12.** B1&B2 test results for web cracks with reference to the maximum principal effective notch stress obtained from the FE-analysis, and according to EN1993–1–9 for combined stress ranges.

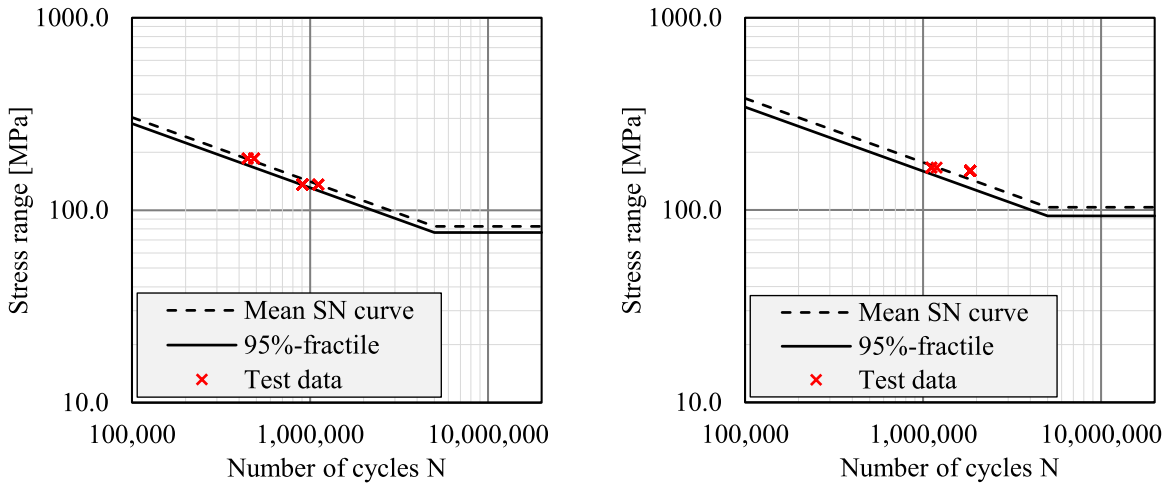


**Fig. 13.** Statistical evaluation of the test data with the nominal stress method.

As shown, all test results lie above the DC100 curve. However, the DC100 appears overly conservative for Group C, where the notch effect is less significant than in Group B (the stress concentration factor for Group C is 1.2, compared to 1.36 for Group B, see Table 6). Moreover, for Group C, the detail category determined using the nominal stress method exceeds DC100 with the HSS method, indicating that the HSS approach becomes increasingly conservative as the notch effect diminishes.

Similarly, all flange cracks that developed in both the pure bending region and the combined shear and bending region were evaluated using

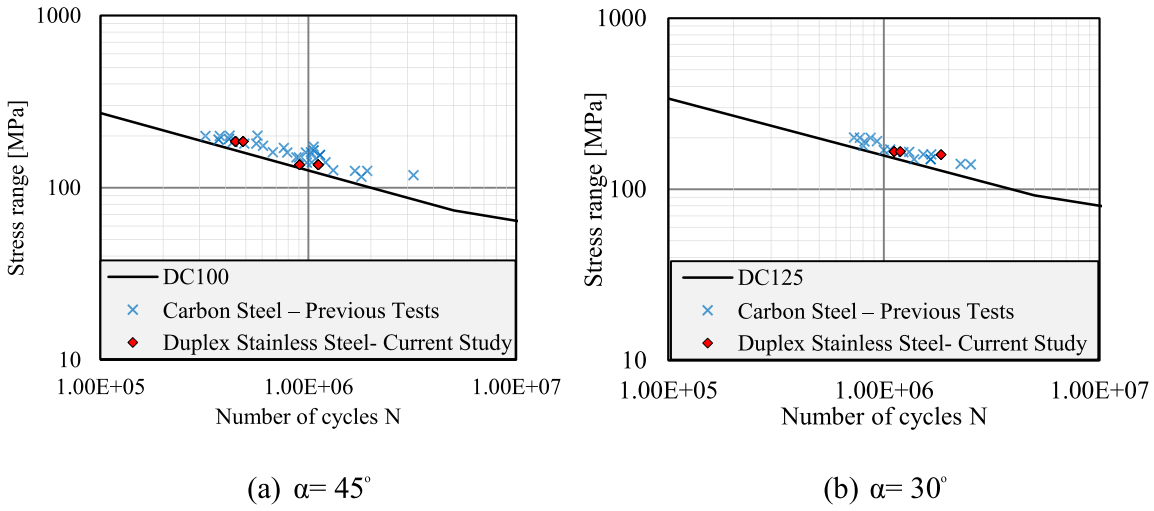


**Fig. 14.** Comparison of previous carbon steel test data and current tests on duplex stainless steel EN 1.4162, plotted with EC3 standard detail categories. Carbon steel data are sourced from Wang et al# [13], Tong et al# [14], and Wang et al# [30] for α= 45° and from Kotaki et al# [31] and Wang et al# [13] for α= 30°.

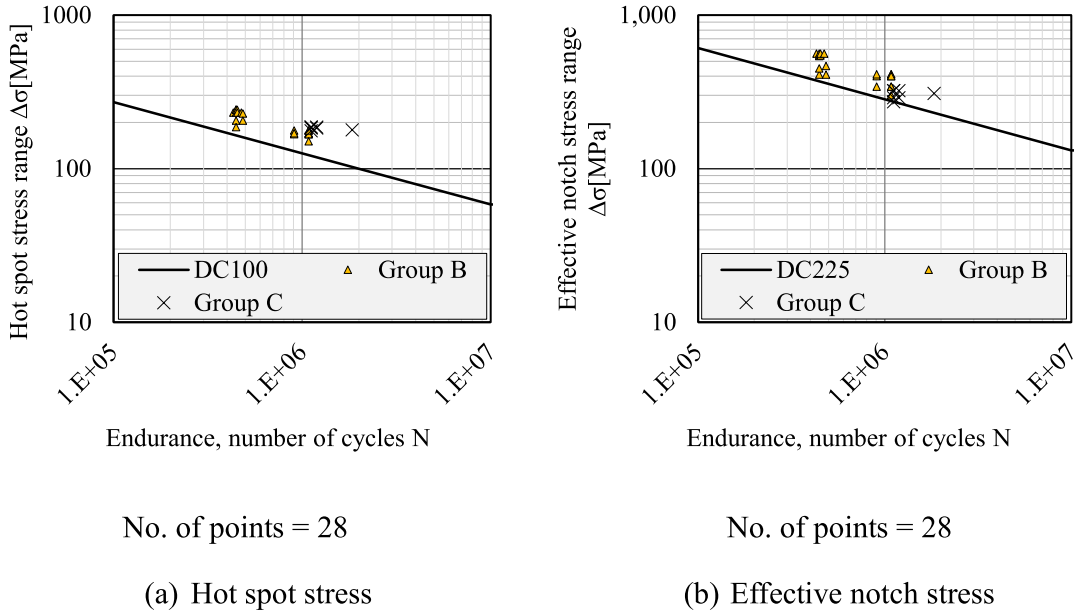


**Fig. 15.** Experimental data with HSS from FE-analysis. Maximum principal stress component.

the ENS method. The ENS values were obtained from numerical analysis, as explained in Section ↱3. As for the hot spot, the ENS & HSS submodels were moved to the crack location, and the corresponding effective notch stress was derived. The results are presented in terms of maximum principal stresses in Fig. 15b. Notably, all test data points lie above the DC225 fatigue class recommended by IIW for effective notch stress in the as-welded condition, indicating that this method can predict the fatigue life of the flange-to-web welded detail in corrugated web beams.

## 6. Summary and conclusions

This paper presented an experimental study on the fatigue behaviour of trapezoidal corrugated web I-girders made of duplex stainless steel (EN 1.4162). Thirteen beams, divided into two groups with different corrugation geometries, were tested to failure under cyclic loading. In addition, one beam from each group was subjected to static loading with strain measurements to estimate the hot spot stress, which was then used to validate the FE model. The test results were evaluated using the nominal stress method as well as the hot spot and effective notch stress methods. The main conclusions are as follows:

- Two distinct cracking modes were observed. Web cracking initiates from the web weld line, and flange cracking initiates at the S-point.
- The tested stainless-steel girders exhibited similar fatigue strength to their carbon steel counterparts. Beams with a 45° corrugation angle conformed to DC100, while those with around a 30° angle conformed to DC125.
- This difference in fatigue strength is the result of decreasing the corrugation angle from 45° to around 30° and increasing the bend radius from 30 mm to 100 mm, which resulted in decreasing the SCF from 1.36 for Group B to 1.2 for Group C, as estimated from test measurements.

- DC100 for the hot spot stress method and DC225 for the effective notch stress method, both according to IIW and based on the maximum principal stress, provided conservative estimates of the fatigue strength of the tested beam.
- More research is needed on how the specimen geometry affects local load distortions and fatigue performance.

## CRediT authorship contribution statement

**Fatima Hlal:** Writing – review & editing, Writing – original draft, Visualization, Validation, Software, Methodology, Investigation, Conceptualization. **Mohammad Al-Emrani:** Writing – review & editing, Supervision, Methodology, Funding acquisition, Conceptualization.

## Declaration of Competing Interest

The authors declare that they have no known competing financial interests or personal relationships that could have appeared to influence the work reported in this paper.

## Acknowledgement

This research is conducted as part of the "Material & cost-effective optimized steel structures for long fatigue life - LONGLIFE" project, which is funded by the VINNOVA [Project No. 2022–01614]. Financial assistance is much appreciated.

The authors would also like to acknowledge HiFIT Scandinavia for their assistance in HFMI treatment, as well as Outokumpu, Borga Sp. z o. o., and Swerim for their contributions in supplying materials, beam production, and quality assurance of the tested specimens.

## Data availability

Data will be made available on request.

## References

[1] Sause R, Abbas HH, Wassef WG, Driver RG, Elgaaly M. Corrugated web girder shape and strength criteria. ATLSS Rep ATLSS Rep Number 0318 2003. ⟨http://preserve.lehigh.edu/engr-civil-environmental-atlss-reports/245⟩.
[2] Ibrahim SA-B, El-Dakhakhni WW, Elgaaly M. Fatigue of Corrugated-Web plate girders: analytical study. J Struct Eng 2006. https://doi.org/10.1061/(ASCE)0733-9445(2006)132:9(1381).
[3] Sayed AM, Elaraki YG, Elalaoui O. Experimental and numerical analysis of steel Beams' efficiency with different shapes of corrugated webs under free vibrations. Metals 2022;12. https://doi.org/10.3390/met12060938.
[4] Karabulut B, Ferraz G, Rossi B. Lifecycle cost assessment of high strength carbon and stainless steel girder bridges. J Environ Manag 2021;277:111460. https://doi.org/10.1016/j.jenvman.2020.111460.
[5] Wahlsten J, Heshmati M, Al-Emrani M. Sustainable infrastructure through increased use of stainless steel. White Pap Outokumpu 2018.
[6] Zilli G, Fattorini F, Maiorana E. Application of duplex stainless steel for welded bridge construction in aggressive environment. Int Conf Duplex 2007 Grado Italy 2008. ⟨https://www.researchgate.net/publication/265668326⟩.
[7] Hechler O, Collin P. On the use of duplex stainless steels in bridge construction. Eng Mater Sci 2008. ⟨https://api.semanticscholar.org/CorpusID:53077077⟩.
[8] Säll J, Tiderman A. Maintenance-free material in bridge superstructures: benefits in a cost- and environment prospective in use of stainless steel and directly molded durable concrete. KTH R Inst Technol 2013. https://kth.diva-portal.org/.
[9] Hlal F, Amani M, Al-Emrani M. Stainless steel corrugated web girders for composite road bridges: optimization and parametric studies. Eng Struct 2023;302. https://doi.org/10.1016/j.engstruct.2023.117366.
[10] Hlal F. Stainless steel corrugated web girders for composite road bridges: concept evaluation and flange buckling resistance. Chalmers Univ Technol Tech Rep No ACE 20239 2023. ⟨https://research.chalmers.se/publication/536891⟩.
[11] Hlal, F., Amani, M., Nilsson, P., Hollberg, A., Al-Emrani, M. (2023). Life Cycle Cost and Life Cycle Assessment of Composite Bridge with Flat and Corrugated Webs. ⟨https://onlinelibrary.wiley.com/doi/epdf/10.1002/cepa.2514⟩.
[12] Kövesdi B, Dunai L. Fatigue life of girders with trapezoidally corrugated webs: an experimental study. Int J Fatigue 2014;64:22–32. https://doi.org/10.1016/j.ijfatigue.2014.02.017.
[13] Wang Z, Wang Q. Fatigue assessment of welds joining corrugated steel webs to flange plates. Eng Struct 2014;73. https://doi.org/10.1016/j.engstruct.2014.04.041.
[14] Tong L, Zhao Z, Zuo G, Wang H, Pan C. Experimental study on fatigue behavior of trapezoidal corrugated-web girders based on T-section members. Eng Struct 2024;298. https://doi.org/10.1016/j.engstruct.2023.117078.
[15] Ibrahim SA, El-Dakhakhni WW, Elgaaly M. Fatigue of Corrugated-Web plate girders: experimental study. J Struct Eng 2006;132(9):1371–80. https://doi.org/10.1061/(asce)0733-9445(2006)132:9(1371)#.
[16] Sause R, Abbas HH, Driver RG, Anami K, Fisher JW. Fatigue life of girders with trapezoidal corrugated webs. J Struct Eng 2006. https://doi.org/10.1061/(ASCE)0733-9445(2006)132:7(1070)#.
[17] Hlal F, Al-Emrani M. Load effects in beams with corrugated webs: numerical study. Nord Steel Constr Conf 2024 (NSCC 2024) Swed Inst Steel Constr 2024. https://doi.org/10.5281/zenodo.12210008.
[18] Abbas HH, Sause R, Driver RG. Analysis of flange transverse bending of corrugated web I-girders under in-plane loads. J Struct Eng 2007;133(3):347–55. https://doi.org/10.1061/(ASCE)0733-9445(2007)133:3(347)#.
[19] Kövesdi B, Jáger B, Dunai L. Stress distribution in the flanges of girders with corrugated webs. J Constr Steel Res 2012;79:204–15. https://doi.org/10.1016/j.jcsr.2012.07.023.
[20] Hlal F, Al-Emrani M. Detail categories for the flange-to-web weld detail in corrugated web girders. Eng Struct 2025. https://doi.org/10.1016/j.engstruct.2024.119342.
[21] Zuo G, Tong L, Zhao Z, Wang H, Shi W, Yan Y. Experimental study on fatigue strength of trapezoidal corrugated-web steel girders based on hot spot stress method. ThinWalled Struct 2025;208. https://doi.org/10.1016/j.tws.2024.112814.
[22] EN1993-1-9. (2005). Eurocode 3: Design of steel structures- Part 1-9: Fatigue.
[23] Karabulut B, Rossi Barbara. On the fatigue behavior of duplex and high-strength welded cruciform joints. Eng Struct 2021. https://doi.org/10.1016/j.engstruct.2021.113161.
[24] Karabulut B, Lombaert G, Debruyne D, Rossi B. Experimental and numerical fatigue assessment of duplex welded transversal stiffeners. Int J Fatigue 2020. https://doi.org/10.1016/j.ijfatigue.2020.105498.
[25] Anami K, Sause R, Abbas H. Fatigue of web-flange weld of corrugated web girders: 1. Influence of web corrugation geometry and flange geometry on web-flange weld toe stresses. Int J Fatigue 2005;27(4):373–81. https://doi.org/10.1016/j.ijfatigue.2004.08.006.
[26] SS-EN 1090-2. Execution of steel structures and aluminium structures – part 2: technical requirements for steel structures. Swed Inst Stand 2018.
[27] Hlal F, Al-Emrani M. Load effects for fatigue design of web-to-flange welded detail in corrugated web girders. SEMC 2025 Ninth Int Conf Struct Eng Mech Comput Cape Town South Afr Eng Mater Struct Syst Methods a More Sustain Future 2025. https://doi.org/10.1201/9781003488644-79.
[28] Al-Emrani M. STEEL STRUCTURES course literature – VSM 191. Chalmers Univ Technol Rep ACE 20231 2023.
[29] Drebenstedt K, Euler M. Statistical analysis of fatigue test data according to eurocode 3. Maintenance, Safety, Risk, Management and Life-Cycle Performance of Bridges, Melbourne. Leiden. CRC Press; 2018. p. 2244–51.
[30] Wang Z, Tan L, Wang Q. Fatigue strength evaluation of welded structural details in corrugated steel web girders. Int J Steel Struct 2013;13(4):707–21. https://doi.org/10.1007/s13296-013-4012-z.
[31] Kotaki N, Ichikawa A, Sasaki E, Miki C, Hosaka T. Proposal of ripple web bridge and its fatigue strength. J Jpn Soc Civ Eng 2003. https://doi.org/10.2208/jscej.2004.766_233.